Commun. Math. Res.
doi: 10.4208/cmr.2026-0028

Vol. **x**, No. x, pp. 1-26
x 2026

An ALE-based Numerical Scheme with a Two-Dimensional Riemann Solver for Two-Phase Flows with Non-Equilibrium Pressure

Jianqiao Zhang[1], Wei Yan[1,*] and Xianggui Li[2]

[1] *School of Mathematics, Jilin University, Changchun 130012, P.R. China.*
[2] *School of Applied Science, Beijing Information Science and Technology University, Beijing 100101, P.R. China.*

Received 2 March 2026; Accepted 23 March 2026

Abstract. In this work, a homogeneous two-phase flow model in two-dimensional space is proposed for systems without a sharp interface between phases. The model allows the two phases to coexist within the same domain with distinct pressures, while their local proportions are represented by volume fractions. Within an arbitrary Lagrangian-Eulerian (ALE) framework, a two-dimensional Riemann solver is developed to construct the numerical scheme with novel formulations for numerical fluxes and nodal velocities, ensuring consistency on moving control volumes. Furthermore, a new moving-mesh strategy is designed, in which the evolution of the volume fraction is obtained directly from the geometric motion of the mesh and mass conservation, thereby avoiding solving the non-conservative convective equation with source terms. This enables the incorporation of physical drag models and finite relaxation coefficients, allowing the gradual equilibration of velocity and pressure between the two phases to be calculated. Based on the volume-fraction formulation, a discrete representation of the pressure work term is derived. Finally, a series of numerical experiments are presented to demonstrate the accuracy, stability, and physical consistency of the proposed model and numerical scheme.

AMS subject classifications: 65M08, 76M12, 76T25, 76T15
Key words: Multiphase flows, ALE method, HLLC-2D, moving mesh.

*Corresponding author. *Email addresses:* jqzhang22@mails.jlu.edu.cn (J. Zhang), wyanmath@jlu.edu.cn (W. Yan), lixg@bistu.edu.cn (X. Li)

1 Introduction

Two-phase flows involving solid particles dispersed in compressible gases arise in a wide range of natural and industrial processes, including volcanic eruptions, engine combustion, and high-speed ejecta transport. In such systems, the particle phase and the fluid often coexist without a well-defined material interface, while exhibiting distinct kinematic and thermodynamic behaviors. Accurately modeling the momentum, energy, and possible mass exchanges between the phases remains a challenging task, particularly in the presence of shock waves, strong compressibility, and non-equilibrium effects.

Early studies on gas-particle flows primarily focused on particle-particle collisions and granular dynamics. Pioneering works by Savage and Jenkins [10,20] investigated rapid granular flows by modeling particles as smooth elastic spheres and deriving stress tensors based on kinetic theory. These approaches were later extended to inelastic particles and shear-driven configurations, such as Couette flows, by Lun [11], with further considerations of particle size effects and velocity distributions [6]. Ding *et al.* [5] formulated two-phase models based on the Boltzmann equation, introducing granular temperature to characterize particle collision dynamics.

Subsequent research gradually shifted attention toward the interaction mechanisms between the particle phase and the background fluid. Sinclair *et al.* [22] analyzed gas-particle flows in vertical pipes and quantified the relationship between pressure gradients and phase flow rates. Charles [2] provided a systematic investigation of momentum exchange mechanisms, demonstrating that interphase momentum transfer is governed by drag forces at low particle concentrations and by collisions at higher concentrations. These findings highlighted the necessity of employing different modeling strategies depending on the particle concentration.

At dilute concentrations, particle trajectory methods, in which individual particles are tracked in a Lagrangian manner, have been widely adopted due to their ability to resolve detailed particle dynamics. Representative examples include ejecta modeling in hydrocodes [7] and the development of MP-PIC and CMP-PIC methods [1,13,14,23], which extend applicability from dilute to moderately dense concentration. However, as particle concentration increases, frequent collisions and collective effects render particle-resolved approaches increasingly expensive and less effective. In this condition, multiphase continuum models that treat both phases as interpenetrating fluids become more appropriate, with collision effects embedded into constitutive relations.

Among continuum approaches, homogeneous multiphase flow models based on volume fractions have attracted considerable attention. Saurel *et al.* [19] introduced a unified framework in which all phases are described within a single set of conservation laws augmented by volume fraction variables, enabling the simulation of mixtures without explicitly tracking material interfaces. Such models are particularly suitable for dense gas-particle flows, where the absence of a sharp interface is a defining feature.

In many practical applications, gas-particle flows are further complicated by strong compressibility and the presence of shock waves. Dusty-gas shock tube problems have therefore been extensively studied as benchmark configurations [3, 8, 9, 15, 18]. Beyond idealized test cases, realistic engineering scenarios such as solid rocket motors and combustion chambers involve shock-induced particle ejection, rapid interphase momentum exchange, and complex flow geometries [12, 16, 17]. These problems place stringent demands on numerical schemes in terms of robustness, conservation, and resolution of discontinuities.

In addition to momentum and energy exchange, mass transfer between phases may occur through chemical reactions when temperature and reactant availability permit. Such reactions are often highly localized in space and time, occurring only in a subset of computational cells. Previous studies have mainly addressed single-particle reactions or trajectory-based models [21, 24], while the consistent treatment of reactive processes in dense two-phase flows remains limited, especially within purely Eulerian frameworks where particle histories are difficult to track.

Despite significant progress, several challenges persist in the numerical simulation of dense gas-particle flows. First, allowing non-equilibrium pressures between phases is essential for capturing transient relaxation processes, yet it introduces additional modeling and numerical difficulties. In particular, pressure work terms involving gradients of volume fractions require careful discretization to maintain consistency and stability. Second, conventional Eulerian schemes necessitate solving additional transport equations for volume fractions, which may complicate the coupling with interphase relaxation models. Finally, the differing velocities of the two phases make purely Lagrangian formulations impractical, while standard Eulerian approaches offer limited flexibility in tracking phase-specific dynamics.

To address these issues, we propose a homogeneous two-phase flow model in two dimensions domain within an arbitrary Lagrangian-Eulerian framework. The model allows the two phases to coexist without a sharp interface and to possess distinct pressures, with their relative presence described by volume fractions. A two-dimensional approximate Riemann solver is constructed to define numer-

ical fluxes, together with a novel formulation of nodal velocities that ensures local conservation at mesh vertices. Based on a carefully designed moving-mesh strategy, the evolution of volume fractions is obtained directly from geometric considerations and mass conservation, eliminating the need for solving separate convective equation. This feature enables the use of physically motivated drag laws and finite pressure relaxation coefficient to model the gradual equilibration of velocities and pressures between phases.

Furthermore, the proposed formulation provides a consistent discretization of pressure work terms in the momentum and energy equations based on the volume fraction framework. Owing to the flexibility of the ALE approach, the particle phase can locally degenerate into a Lagrangian description, which greatly facilitates the tracking of particle motion and the modeling of localized mass exchange processes such as chemical reactions. The accuracy and robustness of the model and numerical scheme are demonstrated through a series of representative numerical experiments.

The remainder of this paper is organized as follows. Section 2 presents the governing equations of the homogeneous two-phase model, including the convective equation of volume fraction and pressure relaxation terms. Section 3 describes the ALE-based numerical method, the two-dimensional Riemann solver, computation of volume fraction under the given moving-mesh strategy, and discretization of pressure work terms. Numerical results are reported in Section 4 to validate the proposed approach. Conclusions are drawn in Section 5.

2 Two-phase flow model

In this section, we introduce the two-phase flow model by regarding the high concentration solid particle phase as a fluid.

2.1 Problem statement and assumptions

Consider a dynamical problem defined on a two-dimensional domain Ω composed of a fluid phase and a high-concentration particle phase. The particles are modeled as a continuum and governed by the compressible Euler equations. There is no explicit and well-defined interface between the two phases; instead, they are assumed to be uniformly mixed throughout the domain. Moreover, each phase is allowed to possess its own pressure and velocity field. To characterize the spatial distribution of the tw phases, an additional variable, th volume fraction is defined. Give the assumption as follows:

(1) Both phases are considered as compressible fluid with equation of state $P=P(e,\rho)$.

(2) Each phase is allowed to possess the own pressure field.

(3) The volume fraction of two phases satisfy the condition $\alpha_g+\alpha_p=1$.

2.2 Governing equations

The governing equations of the proposed two-phase model are first presented in the following form. Subsequently, each equation and the associated variables are explained in detail

$$\begin{aligned}&\frac{\partial \alpha_g}{\partial t}+\mathbf{V}_i\cdot\nabla\alpha_g=\mu(P_g-P_p),\\&\frac{\partial \alpha_k\mathbf{U_k}}{\partial t}+\frac{\partial \alpha_k\mathbf{F}_k(\mathbf{U_k})}{\partial x}+\frac{\partial \alpha_k\mathbf{G}_k(\mathbf{U_k})}{\partial y}=\mathbf{S}_k,\end{aligned}\tag{2.1}$$

where $k=g,p$,

$$\mathbf{U}_k=\begin{bmatrix}\rho_k\\ \rho_k u_k\\ \rho_k v_k\\ \rho_k E_k\end{bmatrix},\quad \mathbf{F}_k(\mathbf{U}_k)=\begin{bmatrix}\rho_k u_k\\ \rho_k u_k^2+P_k\\ \rho_k u_k v_k\\ \rho_k E_k u_k+P_k u_k\end{bmatrix},\quad \mathbf{G}_k(\mathbf{U}_k)=\begin{bmatrix}\rho_k v_k\\ \rho_k u_k v_k\\ \rho_k v_k^2+P_k\\ \rho_k E_k v_k+P_k v_k\end{bmatrix},$$

$$\mathbf{S}_g=-\mathbf{S}_p=\begin{bmatrix}0\\ P_i\dfrac{\partial \alpha_g}{\partial x}+F_{dx}\\ P_i\dfrac{\partial \alpha_g}{\partial y}+F_{dy}\\ P_i\mathbf{V}_i\cdot\nabla\alpha_g+\mu P_i(P_g-P_p)+\mathbf{F}_d\cdot(\mathbf{V}_g-\mathbf{V}_p)\end{bmatrix},$$

with subscripts p and g refering to particle and carrier-fluid phases, respectively. For each phase $k=p,g$, ρ_k, $\mathbf{u}_k$, $E_k=(1/2)|\mathbf{u}_k|^2+e_k$, P_k, are density, velocity, energy and pressure, where e_k is the specific internal energy. Moreover, P_i and $\mathbf{V}_i$ denote the mixture pressure and velocity of two phases, respectively. The term $\mathbf{F}_d$ represents the drag force induced by the relative motion between the two phases, while μ denotes the pressure relaxation coefficient. The physical meaning of each term in the governing equations is analyzed in detail below.

2.2.1 Volume fraction and interface-free description

For flows involving high concentrations of particles, the particulate phase is embedded within the fluid phase, and no distinct interface can be identified in the computational domain. The proposed model is therefore designed for interface-free two-phase flows, in which the volume fraction is introduced to describe the spatial distribution of the phases.

For each phase, the dynamics are described by the compressible Euler equations, with each phase possessing its own pressure, velocity, and density. When source terms and volume fraction effects are neglected, the governing equations for both phases reduce to conservative hyperbolic systems, which can be solved independently. In each computational cell, the mass, momentum, and energy of both phases are computed according to their local volume fractions.

2.2.2 Pressure and velocity relaxation

In many practical flow conditions, the two phases may exhibit significantly different initial states and therefore possess distinct pressures. Under the action of pressure differences, it is physically reasonable for the volume fractions of the two phases to evolve in space and gradually approach an equilibrium state.

The first equation in system (2.1) describes one of the dominant mechanisms driving volume equilibration between the phases. This equation is a convective, non-conservative equation and thus requires special treatment in the numerical solution of the coupled system. The corresponding numerical strategy is detailed in subsequent sections.

Owing to the non-equilibrium of pressure, variations in the volume fraction may occur even in the absence of interphase mass transfer. Consequently, additional pressure work terms must be incorporated into the right sides of the momentum and energy equations until pressure equilibrium between the two phases is attained.

An extra term, denoted by $\mu P_i(P_g - P_p)$, appears in the energy equation only. This term represents the contribution of pressure relaxation to the internal energy and does not affect the momentum balance.

The relaxation of phase velocities toward equilibrium is primarily driven by interphase drag, which facilitates momentum and energy exchange between the two phases. While viscous effects are neglected in the intrinsic dynamics of the fluid phase, they cannot be ignored when modeling interphase drag. The drag force between the phases originates from both the intrinsic viscosity of the carrier fluid and the relative velocity between the fluid and particulate phases. Commonly used drag models for dense partic flow include Wen and Yu model, Gidaspow model, and Syamlal O'Brien model. In this work, the interphase drag

force is modeled by the widely used Gidaspow model, which provides a robust structure over both dilute and dense particle flow by recovering the Wen-Yu drag law at high gas volume fractions and the Ergun (packed-bed) limit at low fractions. The drag force is written in the standard form

$$\mathbf{F}_d = K_{pg}(\mathbf{u}_g - \mathbf{u}_p),$$

where $\mathbf{u}_g$ and $\mathbf{u}_p$ denote the velocities of the fluid and particle phases, respectively, and K_{pg} is the interphase momentum-exchange coefficient. In the Gidaspow model, K_{pg} is defined piecewise as

$$K_{pg} = \begin{cases} K_{WY}, & \alpha_g > 0.8, \\ K_{Ergun}, & \alpha_g \leq 0.8 \end{cases}$$

with

$$\begin{aligned} K_{WY} &= \frac{3}{4}\frac{\rho_g \alpha_g \alpha_p}{d_p} C_D |\mathbf{u}_g - \mathbf{u}_p| \alpha_g^{-2.65}, \\ C_D &= \frac{24}{\alpha_g Re_p}\left[1 + 0.15(\alpha_g Re_p)^{0.687}\right], \\ K_{Ergun} &= 150\frac{\mu_g(1-\alpha_g)^2}{\alpha_g d_p^2} + 1.75\frac{\rho_g(1-\alpha_g)}{d_p}|\mathbf{u}_g - \mathbf{u}_p|. \end{aligned}$$

Here α_g and α_p are the volume fractions ($\alpha_g + \alpha_p = 1$), d_p is the particle diameter, and ρ_g and μ_g are the density and dynamic viscosity of the fluid phase. The particle Reynolds number is defined by

$$Re_p = \frac{\rho_g d_p |\mathbf{u}_g - \mathbf{u}_p|}{\mu_g}.$$

3 Numerical method

In this section, we propose a cell-centered arbitrary Lagrangian-Eulerian numerical scheme for the above equations. A two-dimensional Riemann solver, referred to as HLLC-2D, is introduced as an extension of the classical HLLC approximate solver for the evaluation of numerical fluxes across element interfaces.

Under the requirement of global conservation, a consistent formulation for the nodal velocity is developed, based on which the wave speed of the contact discontinuity is defined. The numerical fluxes on each side of a cell edge are

computed independently from the initial states of the adjacent cells, allowing for unequal fluxes across the same edge. As a consequence, the conservation of mass, momentum, and energy is enforced at the nodal level rather than within individual cells.To solve the coupled system, the second equation in (2.1) are split into two hyperbolic subsystems, which are treated separately within the proposed framework.

For the first equation in system (2.1), governing the evolution of the volume fraction, a specialized moving-mesh velocity is employed. Under this moving mesh strategy, the non-conservative equation does not need to be solved explicitly; instead, the volume fraction at the next time level can be obtained directly. In addition, a discrete formulation of the pressure work term is presented, and the selection of the relaxation coefficient μ is analyzed.

3.1 ALE scheme

For convenience, rewrite the Eq. (2.1) into single hyperbolic equations system for two phases. And each phase has the following two-dimensions and moving control volume formulation:

$$\begin{aligned}&\frac{\partial \alpha \mathbf{U}}{\partial t}+\frac{\partial \alpha \mathbf{F}(\mathbf{U})}{\partial x}+\frac{\partial \alpha \mathbf{G}(\mathbf{U})}{\partial y}=\mathbf{S},\\&\frac{d}{dt}\int_{\Omega}\alpha \mathbf{U}dxdy+\int_{\partial\Omega}\left[(\alpha \mathbf{F},\alpha \mathbf{G})\mathbf{N}-(\mathbf{w}\cdot\mathbf{N})\alpha \mathbf{U}\right]dl=\int_{\Omega}\mathbf{S}dxdy,\end{aligned}\tag{3.1}$$

where $\mathbf{w}$ denotes the mesh moving velocity of the control volume Ω while $\mathbf{N}$ denotes the unit outward normal direction along the boundary of Ω. When $\mathbf{w}=\mathbf{u}$, the system simplifies into a Lagrangian formulation, and when $\mathbf{w}=\mathbf{0}$, it takes on an Eulerian form. In the following part, the choice of $\mathbf{w}$ is discussed to track the volume fraction of two phases in elements.

3.1.1 Notations on a generic polygonal grid

The index c is given as a subscript for any element Ω_c. Then there is a index d representing the adjacent cell Ω_d sharing a common edge with Ω_c and the common edge of two elements is defined $k=c\cap d$, as shown in Fig. 1. $F(c)$ denotes the set of all adjacent cells and $Q(c)$ is the set of all vertices of the cell Ω_c. We use index q to represent the vertex in the mesh while analyzing, and $C(q)$ and $K(q)$ denote the sets of cells and edges respectively containing the vertex q, i.e.,

$$\begin{aligned}C(q)&=\{\Omega_c : \text{cells containing the vertex } q\},\\K(q)&=\{k : \text{edges containing the vertex } q\}.\end{aligned}$$

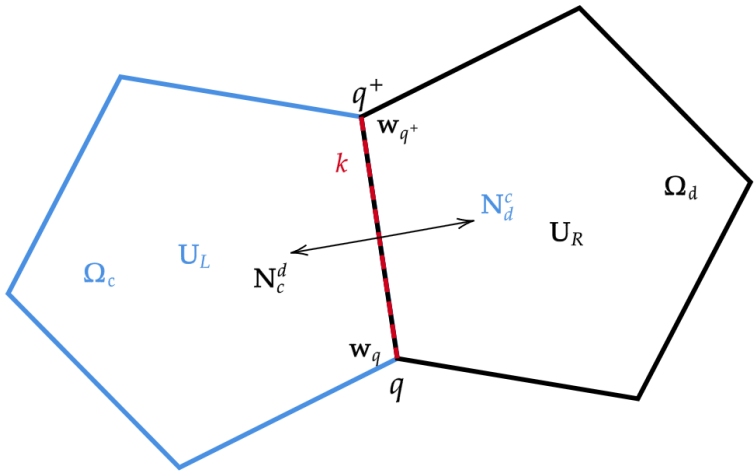

Figure 1: Notations on a grid.

The physical quantities of two phases for example the density ρ_{g_c}, pressure P_{g_c}, velocity v_{g_c}, energy E_{g_c},e_{g_c} are cell-centered, defined in the center of Ω_c while the moving velocity $\mathbf{w}_q$ is defined at the node q. Let $\mathbf{N}_d^c=((n_x)_d^c,(n_y)_d^c)$ represent the unit normal vector of cell Ω_c along edge $c\cap d$ and $\mathbf{N}_d^c=-\mathbf{N}_c^d$.

On either side of any given edge, we utilize indices L and R to represent the states on the left and right sides of an edge, respectively. For instance, $\mathbf{U}_L$ and $\mathbf{U}_R$ are state vectors in the left and right cells of the edge $c\cap d$. To compute integration of the flux across edge $[M_a,M_{a+1}]$, denote by $\mathbf{F}_{a,a+1}$ the fluxes on the face, $L_{a,a+1}$ is the length of $[M_a,M_{a+1}]$, we have

$$L_{a,a+1}\mathbf{F}_{a,a+1}\cdot\mathbf{N}_{a,a+1}=\int_{M_a}^{M_{a+1}}\mathbf{F}\cdot\mathbf{N}\mathrm{d}l.$$

Using the above transformation, we discretize the Eqs. (3.1) by utilizing the Godunov scheme on an unstructured mesh. On any give element Ω_c, we could get the following form:

$$\begin{aligned}\left|\Omega_c^{n+1}\right|\alpha_c\mathbf{U}_c^{n+1}&=|\Omega_c^n|\alpha_c\mathbf{U}_c^n+\Delta t|\Omega_c^n|\mathbf{S}_c^n\\&\quad-\Delta t\sum_d\int_d(\mathcal{T}_d^c)^{-1}\alpha_c[\mathbf{F}(\mathcal{T}_d^c\mathbf{U})-(\mathbf{w}_d^c\cdot\mathbf{N}_d^c)\mathcal{T}_d^c\mathbf{U}]dl\\&=|\Omega_c^n|\alpha_c\mathbf{U}_c^n+\Delta t|\Omega_c^n|\mathbf{S}_c^n\\&\quad-\Delta t\sum_d L_d^c(\mathcal{T}_d^c)^{-1}\alpha_c\mathbf{F}_d^c(\mathbf{w}_d^c\cdot\mathbf{N}_d^c,\mathcal{T}_d^c\mathbf{U}_c,\mathcal{T}_d^c\mathbf{U}_d),\end{aligned}\tag{3.2}$$

where $|\Omega_c|$ represent the volume of cell Ω_c. $\mathbf{w}_d^c$ is the moving velocity defined at the center of cell edge $c\cap d$. L_d^c is the length of the edge $c\cap d$. $\mathcal{T}_d^c$ and $(\mathcal{T}_d^c)^{-1}$ are the rotation matrix and its inverse as follows:

$$\mathcal{T}_d^c=\begin{pmatrix}1 & 0 & 0 & 0\\ 0 & (n_x)_d^c & (n_y)_d^c & 0\\ 0 & -(n_y)_d^c & (n_x)_d^c & 0\\ 0 & 0 & 0 & 1\end{pmatrix},\quad (\mathcal{T}_d^c)^{-1}=\begin{pmatrix}1 & 0 & 0 & 0\\ 0 & (n_x)_d^c & -(n_y)_d^c & 0\\ 0 & (n_y)_d^c & (n_x)_d^c & 0\\ 0 & 0 & 0 & 1\end{pmatrix}.$$

Calculate the approximate numerical flux $\mathbf{F}_d^c$ through solving a one-dimensional Riemann problem along the normal direction of edge $c\cap d$ as follows:

$$\begin{aligned}&\mathbf{U}_t+\mathbf{F}_x=\mathbf{S}_p,\\ &\mathbf{U}(x,0)=\begin{cases}\mathbf{U}_L=\mathcal{T}_d^c\mathbf{U}_c, & x<0,\\ \mathbf{U}_R=\mathcal{T}_d^c\mathbf{U}_d, & x>0,\end{cases}\end{aligned}\tag{3.3}$$

and the numerical flux can be represented as follows:

$$\mathbf{F}_d^c(w,\mathbf{U}_L,\mathbf{U}_R)=\mathbf{F}^w-w\mathbf{U}^w,\tag{3.4}$$

where $w=\mathbf{w}_d^c\cdot\mathbf{N}_d^c$ is the normal projection of the moving velocity $\mathbf{w}_d^c$, $\mathbf{U}^w$ and $\mathbf{F}^w$ are the projection of the state and flux functions onto the direction $x/t=w$ respectively.

3.1.2 Flux formula of HLLC-2D on moving mesh

In this section, a two-dimensional approximate Riemann solver, referred to as HLLC-2D, is developed for the evaluation of numerical fluxes. The construction of this solver relies on two key ingredients.

First, a flux formulation based on the nodal velocity $\mathbf{u}_q^*$ is introduced, in which the numerical fluxes across edges belonging to $K(q)$ are not required to be equal when evaluated from the left and right states. Second, the nodal velocity is computed by enforcing conservation around each vertex under the proposed flux formulation. This procedure guarantees the consistency between the nodal velocity and the numerical fluxes.

In the following evaluation, assume that the nodal contact velocity $\mathbf{u}_q^*$ has already been calculated. From the Riemann problem (3.3), the initial values of the equation are

$$\mathbf{U}_L=\mathcal{T}_d^c\mathbf{U}_c,\quad \mathbf{U}_R=\mathcal{T}_d^c\mathbf{U}_d,$$

and the fluxes are $\mathbf{F}_L=\mathbf{F}(\mathbf{U}_L)$, $\mathbf{F}_R=\mathbf{F}(\mathbf{U}_R)$.

Different from the classical one-dimensional Riemann solver, HLLC-2D method deviates by introducing an artificial contact discontinuity wave speed denoted as $S_* = \mathbf{u}_q^* \cdot \mathbf{N}_d^c$, which is consistent with the nodal velocity $\mathbf{u}_q^*$. Then define two velocities S_L and S_R and suppose $S_L \leqslant S_* \leqslant S_R$. As a result, the HLLC-2D solver comprises 4 constant state regions separated by S_L, S_* and S_R. Within these regions, the vector of conservation quantities is defined as follows:

$$\mathbf{U}^w = \begin{cases} \mathbf{U}_L, & \text{if} \quad w \leqslant S_L, \\ \mathbf{U}_L^*, & \text{if} \quad S_L < w \leqslant S_*, \\ \mathbf{U}_R^*, & \text{if} \quad S_* < w \leqslant S_R, \\ \mathbf{U}_R, & \text{if} \quad w > S_R, \end{cases}$$

where $\mathbf{U}_L^*$, $\mathbf{U}_R^*$ are

$$\mathbf{U}_K^* = \rho_K \frac{S_K - u_K}{S_K - S_*} \begin{bmatrix} 1 \\ S_* \\ v_K \\ E_K + (S_* - u_K)\left(S_* + \dfrac{p_K}{\rho_K (S_K - u_K)}\right) \end{bmatrix}$$

with $K = L,R$. And the new approximate fluxes given which are from the different direction of the edge $c \cap d$

$$\mathbf{F}_H^w = \begin{cases} \mathbf{F}_{H,1}, & \text{if} \quad w \leqslant S_L, \\ \mathbf{F}_{H,2}, & \text{if} \quad S_L < w \leqslant S_*, \\ \mathbf{F}_{H,3}, & \text{if} \quad S_* < w \leqslant S_R, \\ \mathbf{F}_{H,4}, & \text{if} \quad w > S_R, \end{cases} \tag{3.5}$$

where $H = L,R$, and the above flux scheme strictly satisfies the Rankine-Hugoniot conditions. We have

$$\begin{aligned} &\mathbf{F}_{L,2} - \mathbf{F}_{L,1} = S_L (\mathbf{U}_L^* - \mathbf{U}_L) = \mathbf{F}_{R,2} - \mathbf{F}_{R,1}, \\ &\mathbf{F}_{L,3} - \mathbf{F}_{L,2} = S_* (\mathbf{U}_R^* - \mathbf{U}_L^*) = \mathbf{F}_{R,3} - \mathbf{F}_{R,2}, \\ &\mathbf{F}_{L,4} - \mathbf{F}_{L,3} = S_R (\mathbf{U}_R - \mathbf{U}_R^*) = \mathbf{F}_{R,4} - \mathbf{F}_{R,3}. \end{aligned}$$

The wave velocity S_* has been proposed above and only fluxes $\mathbf{F}_{L,1}$ and $\mathbf{F}_{R,4}$ need to satisfy the boundary conditions $\mathbf{F}_{L,1} = \mathbf{F}_L$, $\mathbf{F}_{R,4} = \mathbf{F}_R$. Consequently numerical fluxes across edges around the vertex q according to the Eqs. (3.4) and (3.5) are as

follows:

$$\begin{aligned}
\mathbf{F}^c_{d,q}(w,\mathbf{U}_L,\mathbf{U}_R) &= \mathbf{F}^w_L - w\mathbf{U}^w \\
&= \begin{cases} \mathbf{U}_L(u_L-w)+\mathbf{D}_L, & \text{if} \quad w \leqslant S_L, \\ \mathbf{U}^*_L(S_*-w)+\mathbf{D}^*_L, & \text{if} \quad S_L < w \leqslant S_*, \\ \mathbf{U}^*_R(S_*-w)+\mathbf{D}^*_L, & \text{if} \quad S_* < w \leqslant S_R, \\ \mathbf{U}_R(u_R-w)+\mathbf{D}_R-\mathbf{D}^*_R+\mathbf{D}^*_L, & \text{if} \quad w > S_R, \end{cases} \\
\mathbf{F}^d_{c,q}(w,\mathbf{U}_L,\mathbf{U}_R) &= \mathbf{F}^w_R - w\mathbf{U}^w \\
&= \begin{cases} \mathbf{U}_L(u_L-w)+\mathbf{D}_L-\mathbf{D}^*_L+\mathbf{D}^*_R, & \text{if} \quad w < S_L, \\ \mathbf{U}^*_L(S_*-w)+\mathbf{D}^*_R, & \text{if} \quad S_L \leqslant w < S_*, \\ \mathbf{U}^*_R(S_*-w)+\mathbf{D}^*_R, & \text{if} \quad S_* \leqslant w < S_R, \\ \mathbf{U}_R(u_R-w)+\mathbf{D}_R, & \text{if} \quad w \geqslant S_R, \end{cases}
\end{aligned} \tag{3.6}$$

where $\mathbf{D}_H=(0,P,0,Pu)^T$, $\mathbf{D}^*_H=(0,P^*_H,0,P^*_H S_*)^T$ and pressures are

$$\begin{aligned}
P^*_L &= p_L+\rho_L(S_L-u_L)(S_*-u_L), \\
P^*_R &= p_R+\rho_R(S_R-u_R)(S_*-u_R).
\end{aligned} \tag{3.7}$$

Thus, four fluxes can be obtained on each edge according to the scheme above, with two fluxes on each side shown in Fig. 2. Finally the flux on each side is averaged, resulting in

$$\mathbf{F}^c_d(w,\mathcal{T}^c_d\mathbf{U}_c,\mathcal{T}^c_d\mathbf{U}_d)=\frac{1}{2}\left(\mathbf{F}^c_{d,q}\left(\mathbf{w}_q\cdot\mathbf{N}^c_d,\mathcal{T}^c_d\mathbf{U}_c,\mathcal{T}^c_d\mathbf{U}_d\right)+\mathbf{F}^c_{d,q^+}\left(\mathbf{w}_{q^+}\cdot\mathbf{N}^c_d,\mathcal{T}^c_d\mathbf{U}_c,\mathcal{T}^c_d\mathbf{U}_d\right)\right).$$

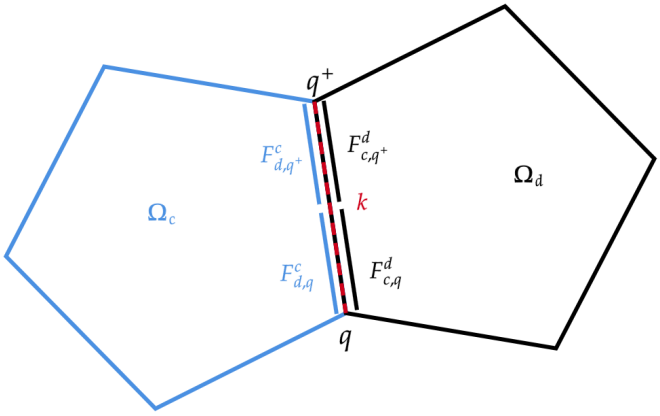

Figure 2: Fluxes on edge q—q^+.

3.1.3 Nodal solver

Since $\mathbf{F}_d^c \neq \mathbf{F}_c^d$ may happen because of the definition of (3.5), the conservation in cells is not always true. Therefore, the computation of nodal velocity $\mathbf{u}_q^*$ should ensure the scheme preserving the local conservation around vertex q and global conservation in Ω. Specifically, the sum of fluxes at all half-edges controlled by vertex q equals zero. Integrate the state function in Ω

$$\begin{aligned}
\frac{d}{dt}\int_\Omega \mathbf{U}dxdy &\approx \frac{1}{\Delta t}\sum_c \left(|V_c^{n+1}|\mathbf{U}_c^{n+1} - |V_c^n|\mathbf{U}_c^n\right) \\
&= -\sum_c \sum_{f\in\mathcal{F}(c)} L_f^c \left(\mathcal{T}_f^c\right)^{-1} \mathbf{F}_f^c \left(\mathbf{w}\cdot\mathbf{N}_f^c, \mathcal{T}_f^c\mathbf{U}_c, \mathcal{T}_f^c\mathbf{U}_f\right) \\
&= -\frac{1}{2}\sum_q \sum_{c\in\mathcal{C}(q)} \Big[L_{c^+}^c \left(\mathcal{T}_{c^+}^c\right)^{-1} \mathbf{F}_{c^+,q}^c \left(\mathbf{w}_q\cdot\mathbf{N}_{c^+}^c, \mathcal{T}_{c^+}^c\mathbf{U}_c, \mathcal{T}_{c^+}^c\mathbf{U}_{c^+}\right) \\
&\qquad + L_{c^-}^c \left(\mathcal{T}_{c^-}^c\right)^{-1} \mathbf{F}_{c^-,q}^c \left(\mathbf{w}_q\cdot\mathbf{N}_{c^-}^c, \mathcal{T}_{c^-}^c\mathbf{U}_c, \mathcal{T}_{c^-}^c\mathbf{U}_{c^-}\right)\Big] \\
&\equiv -\frac{1}{2}\left(\sum_{q\in\mathcal{I}(\Omega)}\sum_{c\in\mathcal{C}(q)} \mathbf{FF}_{c,q} + \sum_{q\in\mathcal{B}(\Omega)}\sum_{c\in\mathcal{C}(q)} \mathbf{FF}_{c,q}\right),
\end{aligned}$$

where $\mathcal{B}(\Omega)$ is the set of boundary nodes while $\mathcal{I}(\Omega)$ is of inner nodes. Indeed a sufficient condition for conservation is

$$\sum_{c\in\mathcal{C}(q)} \mathbf{FF}_{c,q} = 0. \tag{3.8}$$

Plug the flux definition into (3.8) and utilize the wave contact discontinuity velocity $S_* = \mathbf{u}_q^*\cdot\mathbf{N}_d^c$ and the pressure equation (3.7), we have

$$\sum_{k\in K(q)} L_k(\alpha_{L,k}+\alpha_{R,k})\left[\mathbf{u}_q^*\cdot\mathbf{N}_k - v_k^*\right]\mathbf{N}_k = 0, \tag{3.9}$$

where

$$\alpha_{L,k} = -\rho_{L,k}(S_{L,k}-u_{L,k}), \quad \alpha_{R,k} = \rho_{R,k}(S_{R,k}-u_{R,k}),$$

and v_k^* represents the contact velocity in the classical one-dimensional HLLC Riemann solver for edge k

$$v_k^* = \frac{P_{L,k} - P_{R,k} + \alpha_{L,k}u_{L,k} + \alpha_{R,k}u_{R,k}}{\alpha_{L,k}+\alpha_{R,k}}.$$

Solve the Eq. (3.9) to calculate the contact velocity $\mathbf{u}_q^*$ at each vertex and we have

$$\mathbf{u}_q^* = M^{-1} \sum_{k\in K(q)} L_k(\alpha_{L,k}+\alpha_{R,k}) v_k^* \mathbf{N}_k, \tag{3.10}$$

where

$$M = \begin{bmatrix} \sum_{k\in K(q)} L_k(\alpha_{L,k}+\alpha_{R,k}) n_{x,k}^2 & \sum_{k\in K(q)} L_k(\alpha_{L,k}+\alpha_{R,k}) n_{x,k} n_{y,k} \\ \sum_{k\in K(q)} L_k(\alpha_{L,k}+\alpha_{R,k}) n_{x,k} n_{y,k} & \sum_{k\in K(q)} L_k(\alpha_{L,k}+\alpha_{R,k}) n_{y,k}^2 \end{bmatrix}.$$

3.1.4 Time discretization

An explicit scheme is employed for the time discretization of system (3.2). Within this framework, the overall accuracy of the method is primarily determined by the spatial discretization. Consequently, only a first-order time integration is considered in the present work.

To ensure numerical stability and physical admissibility, several constraints on the time step must be imposed. First, a CFL-type condition, denoted by Δt_e, is derived to guarantee positive entropy production within each computational cell Ω_i. At time t^n, we denote by λ_i^n the inner circle radius of the cell Ω_i. Then

$$\Delta t_e = C_e \min_{i=1,\dots,I} \frac{\lambda_i^n}{\sqrt{(u_{g_i}^n)^2+(v_{g_i}^n)^2}+c_i^n},$$

where C_E is a strictly positive coefficient and c_i is the sound speed of the cell Ω_i. Numerically, the value of C_E between 0.3 and 0.4 is usually taken.

Second, a criterion Δt_v is introduced to control the variation of the cell volume during mesh motion. At time t^n, we can get the contact velocity of vertex, we have

$$\Delta t_v = C_V \min_{i=1,\dots,I} \left\{ \frac{|A_i^n|}{|A_i'|} \right\},$$

where C_v can be set 0.1 and

$$|A_i'| = \frac{1}{2} \sum_f L_f^c (\mathbf{u}_q^* + \mathbf{u}_{q^+}^*) \cdot \mathbf{N}_f^c.$$

The time step at the next time level is then estimated as $\Delta t^n = t^{n+1} - t^n$, subject to the above constraints. Since a two-phase system is considered, the CFL condition is evaluated separately for each phase, and the minimum value is adopted as the final time step

$$\Delta t^n = \min\left(\Delta t_e, \Delta t_v, 1.01 * \Delta t^{n-1}\right). \tag{3.11}$$

3.2 Moving velocity and volume fraction

In general, numerical simulations of two-phase flows are predominantly conducted within an Eulerian framework, since the two phases typically possess different velocities, as illustrated in Fig. 3. At time t^n, the fluid phase and the particle phase occupy different volume fractions within the same computational cell Ω_c^n. Over a time step Δt, the two phases evolve independently and are transported to different regions, denoted by $\Omega_{c,g}^{n+1}$ and $\Omega_{c,p}^{n+1}$, as a consequence of their distinct nodal velocities $\mathbf{u}i,g^n$ and $\mathbf{u}i,p^n$, $i=1,2,3,4$. As a result, at time t^{n+1}, the cell composition is altered by the inflow of new gas and particles, and the corresponding volume fractions must be re-evaluated through the first equation in (2.1).

Owing to the velocity disparity between the two phases, a purely Lagrangian formulation is generally not suitable for two-phase flow simulations. However, Eulerian methods require the convective transport of each phase to be computed separately and necessitate the reconstruction of volume fractions in every cell at each time step, which can be cumbersome and computationally inefficient.

In contrast, the present method is formulated within an ALE framework, which allows the grid velocity to be chosen flexibly. In the scheme, the mesh velocity is set equal to the velocity of either phase. For simplicity and clarity, assume that the computational cell Ω_c^n moves with the velocity of the particulate phase, as illustrated in Fig. 4, such that $\Omega_{c,p}^{n+1}=\Omega_c^{n+1}$. In this configuration, the proposed scheme effectively reduces to a Lagrangian formulation for the particle phase, which facilitates the tracking of particle motion, while retaining a standard ALE formulation for the gas phase. For the gas phase, the convective terms are evaluated directly using the discretization given in (3.2). This hybrid treatment provides the flexibility needed to efficiently simulate a wide range of two-phase flow problems.

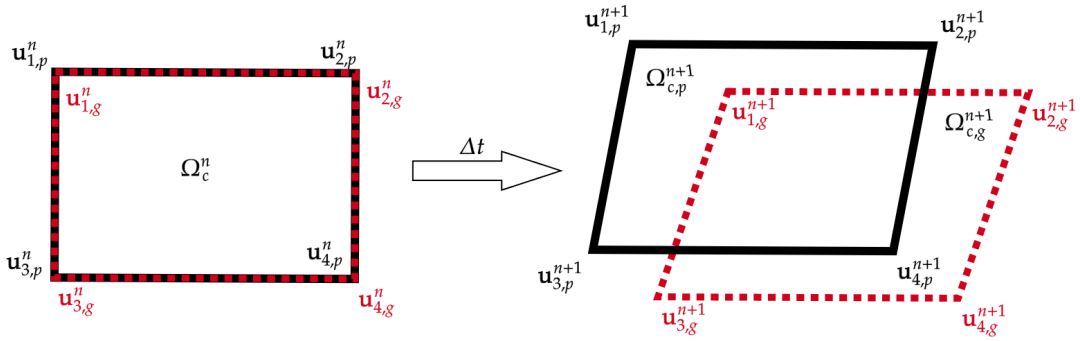

Figure 3: Motion of two phases (black is particle, red is gas).

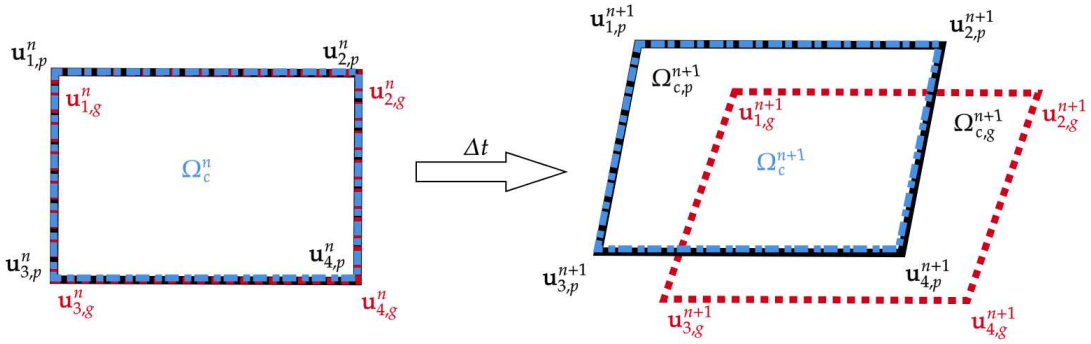

Figure 4: $\mathbf{w}=\mathbf{u}^n_{i,p}$ and $\Omega^{n+1}_{c,p}=\Omega^{n+1}_c$ (blue is element c).

Under this choice, the updated volume fractions within the cell Ω^{n+1}_c can be obtained naturally without explicitly solving the non-conservative volume fraction equation as follows:

$$\alpha^{n+1}_{c,p}=\frac{\alpha^n_{c,p}|\Omega^n_c|\rho^n_{c,p}}{|\Omega^{n+1}_c|\rho^{n+1}_{c,p}}, \tag{3.12}$$

$$\alpha^{n+1}_{c,g}=1-\alpha^{n+1}_{c,p}, \tag{3.13}$$

where $\rho^{n+1}_{c,p}$ and $|\Omega^{n+1}_c|$ could be obtained by solving the hyperbolic equations.

An additional advantage of the proposed method arises in the modeling of two-phase flows involving interphase mass transfer, such as chemical reactions, which may occur in a highly non-uniform manner across the computational domain. In practice, such processes are often restricted to some limited cells where specific reaction criteria are satisfied, rather than taking place uniformly in space or time.

Within a purely Eulerian framework, the inability to explicitly track particle trajectories makes it difficult to determine which particles have undergone mass transfer, how long the reaction has persisted, and to what extent it has progressed. In contrast, the present formulation allows the particle phase to be treated in a Lagrangian scheme by setting the grid velocity appropriately. This feature enables accurate tracking of particle motion, facilitates the evaluation of reaction conditions along particle trajectories, and provides a natural way to quantify the local extent of mass transfer. As a result, the reaction state of the particulate phase within each computational cell can be characterized more consistently than in Eulerian framework.

3.3 Discretization of pressure work term

The momentum and energy equations contain pressure work terms $P_i\nabla\alpha_k$ and $P_i\mathbf{V}_i\cdot\nabla\alpha_k$ on the right side, which involve gradients of the volume fraction. As a result, the discretization of these terms requires special treatment. For the momentum equation, integrate $P_i\nabla\alpha_k$ over the cell Ω_c and use the divergence theorem

$$\int_{\Omega_c} P_i\nabla\alpha_{k,c}d\Omega_c = P_{i,c}\int_{\Omega_c}\nabla\alpha_{k,c}d\Omega_c = P_{i,c}\int_{\partial\Omega_c}\alpha_{k,c}\mathbf{n}dS.$$

Actually since no well-defined interface exists between the two phases, and the variation of volume fraction over a time step can be regarded as isotropic, no unique normal direction $\mathbf{n}_\alpha$ can be identified. Consequently, the volume fraction boundary integration can be approximated as zero

$$\int_{\partial\Omega_c}\alpha_{k,c}\mathbf{n}dS \approx 0.$$

For the energy equation term, substitute the first equation of system (2.1) into the $P_i\mathbf{V}_i\cdot\nabla\alpha_k$

$$\begin{aligned} P_i\mathbf{V}_i\cdot\nabla\alpha_k &= P_i\left(\mu(P_g-P_p)-P_i\frac{\partial\alpha_g}{\partial t}\right) \\ &= P_i\left(\mu(P_g-P_p)-P_i\left(\alpha_g^{n+1}-\alpha_g^n\right)/\Delta t_n\right). \end{aligned} \tag{3.14}$$

A further issue that requires special attention is the choice of the pressure relaxation coefficient μ. In many traditional two-phase models, μ is often taken to be infinite in order to enforce instantaneous pressure equilibrium. Under this assumption, pressure differences are eliminated solely through the redistribution of volume fractions, and it is an instantaneous process rather than a continuous process. This limitation stems from the fact that the volume fraction evolution is governed by a non-conservative convective equation with source terms.

As shown in the previous section, the present scheme provides a new strategy for computing the volume fraction, thereby removing the necessity of taking $\mu\to\infty$. When μ is finite, the pressure equilibration is no longer achieved exclusively through volumetric rearrangement; instead, the fluid motion of each phase also contributes to the relaxation process. In this case, the value of μ determines the characteristic time scale of pressure equilibration, which should remain consistent with the acoustic time scale of the system.

Two strategies for this time scale are considered: a physical scale and a numerical scale. For the physical scheme, there is

$$\mu = C_p\frac{c_i}{L_p},$$

where c_i is the mixture sound velocity. L_p is a physical scale such as the particle diameter or other relevant physical measures. For the numerical scale

$$\mu = C_p \frac{c_i}{\Delta x},$$

where Δx represents the mesh scale. Under both scaling strategies, short-time pressure non-equilibrium is permitted, while the pressure difference is required to decay gradually within a finite time steps. The decay rate of the pressure difference can be further adjusted through a dimensionless coefficient C_p, which controls the relaxation time.

3.4 Algorithm for full discretization system

Give the conclusion of the whole computation process:

Algorithm 1

1: At time step t_n, initialize the physical variables and solve the equation by (3.2).
2: Calculate the nodal velocities of two phases through (3.10) and cfl contion to get the moving mesh strategy.
3: Solve the numerical fluxes of gas and particle phases at respectively by (3.6).
4: Update the density of two phases and get the volume fraction by (3.12) and (3.13).
5: Calculate the pressure work term and update the velocity, energy and pressure of two phases by (3.14).
6: Check if the final time step is reached; if not, return to the step 1.

4 Numerical tests and results

4.1 Shock-particle-cloud duct problem

To validate the proposed numerical scheme, we consider a classic shock-particle-cloud configuration and analyze the corresponding numerical results. The computational domain is $[0,1]\times[0,0.1]$. An incident shock is introduced from the left boundary, with its initial location set at $x = 0.1$. In this section, we adopt the

numerical-scale definition of the pressure relaxation coefficient μ. The dimensionless parameter C_p is chosen in the range 0.3-0.5, depending on the desired convergence rate of the phase pressures toward equilibrium (larger C_p yields faster convergence).

To mimic a realistic operating condition, a substantially elevated initial pressure is prescribed on the right side of the domain. The post-shock state is determined from the Rankine-Hugoniot jump conditions, while the inflow conditions at the left boundary are held fixed to continuously sustain the incident shock. Suppose that the pre-shock state and post-shock are $[\rho_1,P_1,u_1]=[1.2,101325,0]$ and $[\rho_2,P_2,u_2]$ respectively and the Mach number M_s of shock is given. The gas is ideal and the initial post-shock state on the left side is computed as follows:

$$c_1=\sqrt{\gamma_g P_1/\rho_{g,1}},\quad V_s=M_s c_1$$

with the Rankine-Hugoniot jump conditions, we have

$$\begin{aligned}
&\frac{P_2}{P_1}=1+\frac{2\gamma_g}{\gamma_g+1}\left(M_s^2-1\right),\\
&\frac{\rho_2}{\rho_1}=\frac{\left(\gamma_g+1\right)M_s^2}{\left(\gamma_g-1\right)M_s^2+2},\\
&u_2=V_s\left(1-\frac{\rho_1}{\rho_2}\right),
\end{aligned}$$

and energy is

$$e_2=\frac{P_2}{\left(\gamma_g-1\right)\rho_2},\quad E_2=e_2+\frac{1}{2}u_2^2.$$

Three shock strengths are considered, corresponding to Mach numbers $M_s=1.2$, 1.5, and 1.8. For each case, the pre-shock and post-shock states are determined according to the Rankine-Hugoniot relations. The corresponding left and right states are summarized in Table 1.

Table 1: Post-shock states.

M_s	ρ_2	P_2	u_2
1.2	1.609	153332	104.7
1.5	2.235	249100	238.7
1.8	2.8	366121	356.5

Since the incident shock starts at $x=0.1$ and propagates to the right, a particle cloud is initialized downstream of the shock to model shock-particle-cloud interaction. Specifically, in the region $x\in[0.1,0.2]$, particles are uniformly distributed with initial volume fraction of 0%, 12%, and 50%, respectively.

As a baseline, we first present the fluid solution without particles ($\alpha_p=0$) for the three shock strengths at $t=5.0\times10^{-5}$ s in Fig. 5.

For the intermediate shock strength $M_s=1.2$, we focus on the pressure and velocity responses of the carrier fluid. At $t=5.0\times10^{-5}$ s, the presence of particles leads to noticeable deviations from the particle-free baseline, and the impact becomes more pronounced as the particle volume fraction increases.

As shown in Fig. 6, although the evolution time is relatively short, the velocity and pressure distributions already exhibit clear deviations from the particle-free case. The presence of particles increases the effective inertia and resistance of the mixture, resulting in a delayed fluid motion and a higher post-shock pressure level. In addition, both the fluid density and internal energy are observed to increase, reflecting the enhanced compression and energy accumulation induced by the particle–fluid interaction.

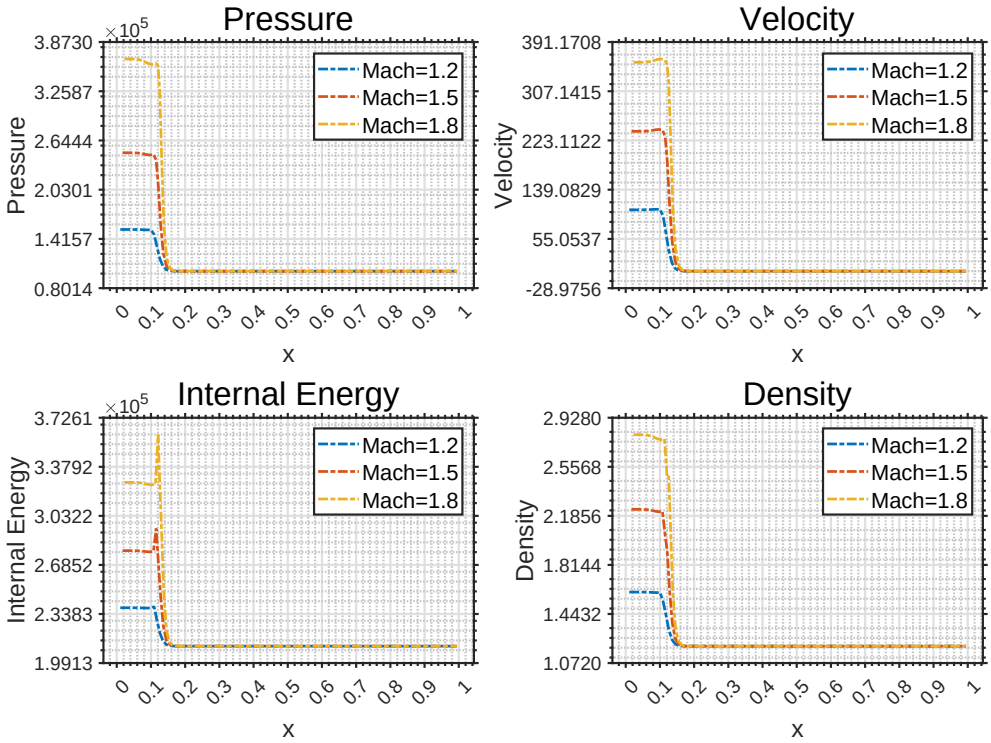

Figure 5: 0% volume fraction with different Mach numbers.

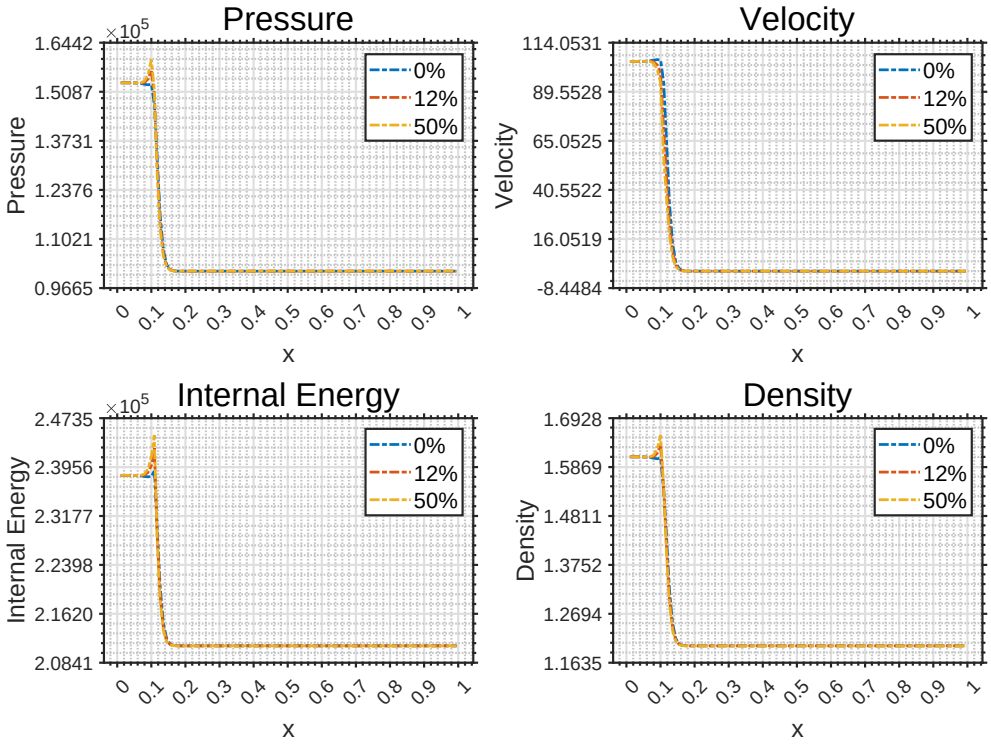

Figure 6: Different volume fractions under $M_s = 1.2$ with $t = 5.0 \times 10^{-5}$ s.

To investigate the cumulative impact of this interaction, the simulation time is extended to $t = 1.0 \times 10^{-4}$ s and focus on the pressure and velocity. The results are displayed in Fig 7.

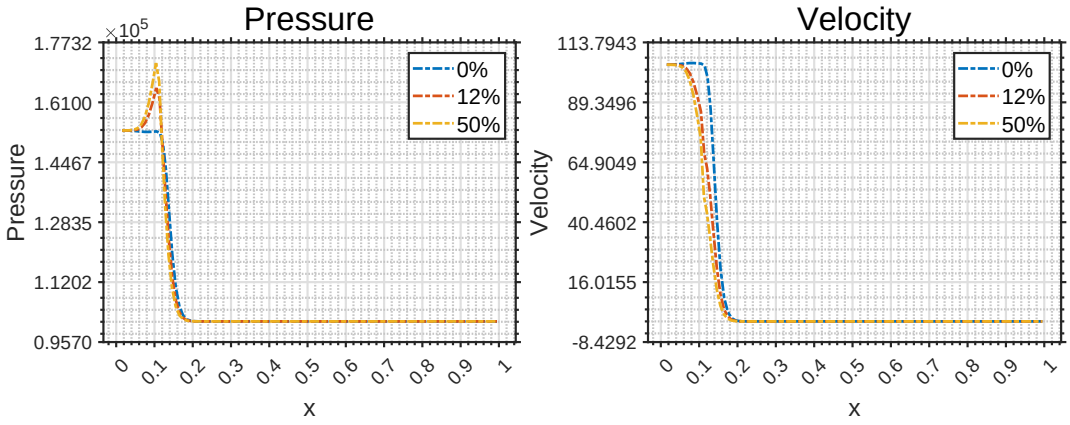

Figure 7: Different volume fractions under $M_s = 1.2$ with $t = 1.0 \times 10^{-4}$ s.

As the simulation time increases, the shock-induced discontinuities become progressively smeared. This smoothing effect becomes more pronounced as the particle volume fraction increases, indicating a stronger effective dissipative influence induced by the particulate phase. These observations are consistent with the dense particle flow results reported in [4].

We examine the velocity and pressure distributions at $t=0.5\times10^{-4}$ s, $t=1.0\times10^{-4}$ s, and $t=2.0\times10^{-4}$ s for the 50% particle volume fractions shown in Fig. 8.

For a fixed particle volume fraction, the flow discontinuities are progressively attenuated as time advances, and the solution becomes increasingly smooth. In particular, the pressure gradually increases in the region where the shock interacts with the particle cloud. Overall, these results indicate that the presence of particles mitigates the impact of the shock on the background fluid, leading to a gradual damping of the shock-induced disturbances.

We next analyze the evolution of the particle volume fraction within each cell. In the present test, the mesh velocity is chosen to coincide with the velocity of fluid phase, and the particle volume fraction is subsequently recomputed based on the resulting mesh motion. As a representative case, consider an initial particle volume fraction of 50%. Fig. 9 illustrates the distribution of cell areas at $t=2.0\times10^{-4}$ s, providing a schematic view of the mesh deformation under the adopted moving-mesh strategy. The cell area is unitless in the sense that its numerical value is determined by the length scale adopted in the mesh coordinates.

Then present the corresponding particle volume fraction distribution at this time instant in Fig. 10.

Since the fluid velocity exceeds that of the particle phase, adopting the fluid velocity as the mesh velocity inevitably leads to a redistribution of particles over a larger number of computational cells. As a consequence, even cells that initially

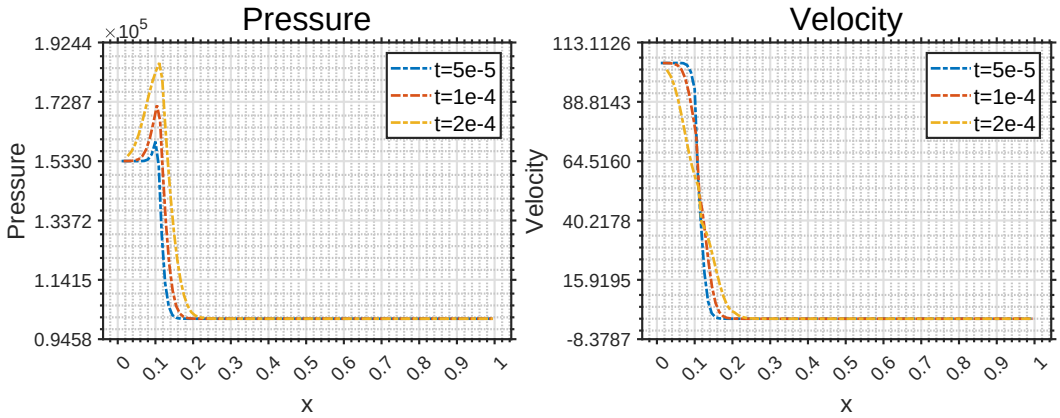

Figure 8: Different time under $M_s=1.2$ with 50% volume fraction.

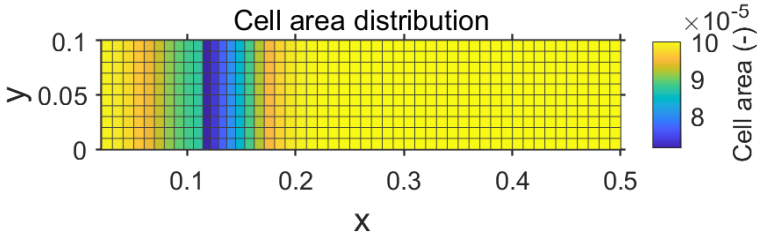

Figure 9: Mesh area.

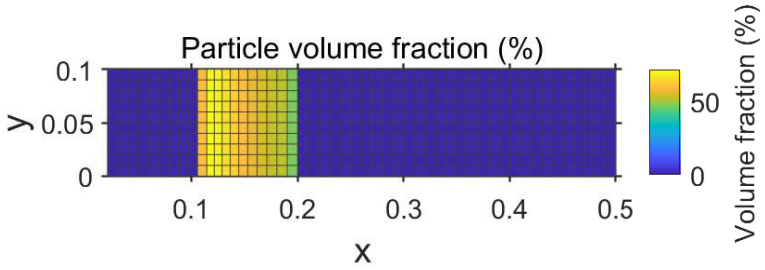

Figure 10: Volume fraction.

contain zero particle volume fraction may exhibit a nonzero volume fraction presence after the evolution.

In regions where the shock intensity is strongest, the mesh cells undergo significant compression due to the fluid motion, resulting in a substantial increase in the local particle volume fraction. In contrast, as the flow propagates further downstream and away from the shock front, the particle volume fraction decreases in those cells and may even fall below the initial uniform value of 50%.

The above numerical example shows that the effects of the particle phase on the global flow evolution are consistently reflected in both the conserved flow quantities and the corresponding volume fraction distribution.

5 Conclusion

In this work, a homogeneous two-phase flow model and an associated numerical method have been developed for the simulation of dense gas-particle flows in two dimensions domain. The proposed model allows the two phases to coexist without a sharp interface and to possess distinct pressures, with their relative presence described by volume fractions. Interphase momentum and energy exchanges are modeled through physically motivated drag and pressure relaxation mechanisms, and the framework naturally accommodates mass transfer processes such as chemical reactions.

A key contribution of this study lies in the construction of an arbitrary Lagrangian-Eulerian numerical scheme for the proposed two-phase model. Within the ALE framework, a two-dimensional approximate Riemann solver, referred to as HLLC-2D, is introduced together with a novel definition of numerical fluxes and nodal velocities. Local conservation of mass, momentum, and energy is enforced around mesh vertices, ensuring consistency between the flux formulation and the nodal motion.

Another important feature of the method is the treatment of volume fractions and pressure work terms. By adopting a carefully designed moving-mesh strategy, the evolution of volume fractions is obtained directly from geometric considerations and mass conservation, avoiding the need to solve additional non-conservative convective equations. This approach enables the use of finite pressure relaxation coefficients, allowing transient pressure non-equilibrium to be resolved in a physically meaningful manner. Based on the volume fraction calculation, a consistent discretization of pressure work terms in the momentum and energy equations is derived, which is essential for maintaining stability and accuracy in non-equilibrium regimes.

The flexibility of the ALE formulation further allows the grid velocity to be chosen to coincide with the velocity of a selected phase, such that the particle phase may locally degenerate into a Lagrangian description while the fluid remains in an standard ALE form. This property is particularly advantageous for modeling localized mass exchange and chemical reactions, where tracking the history and state of particles or fluid is crucial.

A series of numerical experiments has been carried out to demonstrate the accuracy, robustness, and effectiveness of the proposed model and numerical scheme. The results confirm that the method can accurately capture interphase relaxation processes and resolve strong flow features such as shock waves.

Acknowledgments

This research was supported by the National Natural Science Foundation of China (Grant Nos. 12272059, 11871113, 22341302), by the National Key Research and Development Program of China (Grant No. 2020YFA0713602), and by the Key Laboratory of Symbolic Computation and Knowledge Engineering of Ministry of Education of China housed at Jilin University.

References

[1] M. J. Andrews and P. J. O'Rourke, *The multiphase particle-in-cell (MP-PIC) method for dense particulate flows*, Int. J. Multiphase Flow 22 (1996), 379–402.

[2] C. S. Campbell and A. Gong, *The stress tensor in a two-dimensional granular shear flow*, J. Fluid Mech. 164 (1986), 107–125.

[3] S. Carcano, L. Bonaventura, T. Esposti Ongaro, and A. Neri, *A semi-implicit, second-order-accurate numerical model for multiphase underexpanded volcanic jets*, Geosci. Model Dev. 6 (2013), 1905–1924.

[4] D. Chen, *Theoretical Modeling and Numerical Study on the Mixing of Metal Particles with Gas under Detonation Driven Conditions*, Ph.D Thesis, China Academy of Engineering Physics, 2016.

[5] J. Ding and D. Gidaspow, *A bubbling fluidization model using kinetic theory of granular flow*, AIChE J. 36 (1990), 523–538.

[6] M. Farrell, C. Lun, and S. Savage, *A simple kinetic theory for granular flow of binary mixtures of smooth, inelastic, spherical particles*, Acta Mech. 63 (1986), 45–60.

[7] J. Fung, A. K. Harrison, S. Chitanvis, and J. Margulies, *Ejecta source and transport modeling in the FLAG hydrocode*, Comput. Fluids 83 (2013), 177–186.

[8] M. Gurris, D. Kuzmin, and S. Turek, *Finite element simulation of compressible particle-laden gas flows*, J. Comput. Appl. Math. 233 (2010), 3121–3129.

[9] S. Hank, R. Saurel, and O. Le Metayer, *A hyperbolic Eulerian model for dilute two-phase suspensions*, J. Mod. Phys. 2 (2011), 997–1011.

[10] J. T. Jenkins and S. B. Savage, *A theory for the rapid flow of identical, smooth, nearly elastic, spherical particles*, J. Fluid Mech. 130 (1983), 187–202.

[11] C. K. Lun, S. B. Savage, D. Jeffrey, and N. Chepurniy, *Kinetic theories for granular flow: Inelastic particles in Couette flow and slightly inelastic particles in a general flowfield*, J. Fluid Mech. 140 (1984), 223–256.

[12] F. Najjar, A. Haselbacher, S. Balachandar, and R. Moser, *Simulations of droplet nozzle impact and slag accumulation in the RSRM*, in: Proceedings of the 42nd AIAA/ASME/SAE/ASEE Joint Propulsion Conference & Exhibit, (2006), Paper No. 4588.

[13] D. M. Oro, J. E. Hammerberg, W. T. Buttler, F. G. Mariam, C. L. Morris, C. Rousculp, and J. B. Stone, *A class of ejecta transport test problems*, in: Proceedings of the AIP Conference, 1426 (2012), 1351–1354.

[14] S.-I. Pai, *Two-Phase Flows*, Springer-Verlag, 2013.

[15] M. Pelanti and R. J. LeVeque, *High-resolution finite volume methods for dusty gas jets and plumes*, SIAM J. Sci. Comput. 28 (2006), 1335–1360.

[16] A. Ristori and E. Dufour, *Numerical simulation of ducted rocket motor*, in: Proceedings of the 37th Joint Propulsion Conference and Exhibit, 2001, Paper No. 3193.

[17] J. Sachdev, C. Groth, and J. Gottlieb, *A parallel solution-adaptive scheme for multi-phase*

core flows in solid propellant rocket motors, Int. J. Comput. Fluid Dyn. 19 (2005), 159–177.

[18] T. Saito, *Numerical analysis of dusty-gas flows*, J. Comput. Phys. 176 (2002), 129–144.

[19] R. Saurel and R. Abgrall, *A multiphase Godunov method for compressible multifluid and multiphase flows*, J. Comput. Phys. 150 (1999), 425–467.

[20] S. Savage and D. Jeffrey, *The stress tensor in a granular flow at high shear rates*, J. Fluid Mech. 110 (1981), 255–272.

[21] J. Schwarzkopf et al., *Modeling of cerium ejecta in helium and deuterium gases*, in: Proceedings of the AIP Conference, 2272(1) (2020), Paper No. 070042.

[22] J. Sinclair and R. Jackson, *Gas-particle flow in a vertical pipe with particle-particle interactions*, AIChE J. 35 (1989), 1473–1486.

[23] B. Tian, J. Zeng, B. Meng, Q. Chen, X. Guo, and K. Xue, *Compressible multiphase particle-in-cell method (CMP-PIC) for full pattern flows of gas-particle system*, J. Comput. Phys. 418 (2020), Paper No. 109602.

[24] P. Wang, H. Q. Sun, J. L. Shao, C. S. Qin, and X. Z. Li, *Numerical simulation on mixing process of ejecta and gas*, Acta Phys. Sin. 61 (2012), Paper No. 234703.